

# 1 **Physics of Self-Assembly and Morpho-Topological Changes of *Klebsiella*** 2 ***Pneumoniae* in Desiccating Sessile Droplets**

3 Abdur Rasheed<sup>1</sup>, Omkar Hegde<sup>1</sup>, Ritika Chaterjee<sup>2</sup>, Srinivas Rao Sampathirao<sup>1</sup>, Dipshikha  
4 Chakravorty<sup>2</sup>, Saptarshi Basu<sup>1\*</sup>

5 <sup>1</sup>Department of Mechanical Engineering, Indian Institute of Science, Bangalore

6 <sup>2</sup>Department of Microbiology and Cell Biology, Indian Institute of Science, Bangalore

7 \*Corresponding author email – [sbasu@iisc.ac.in](mailto:sbasu@iisc.ac.in)  
8  
9

## 10 **Abstract**

11 We have investigated the flow and desiccation-driven self-assembly of *Klebsiella Pneumoniae*  
12 in the naturally evaporating sessile droplets. *Klebsiella Pneumoniae* exhibits extensive changes  
13 in its morphology and forms unique patterns as the droplet dries, revealing hitherto unexplored  
14 rich physics governing its survival and infection strategies. Self-assembly of bacteria at the  
15 droplet contact line is characterized by order-to-disorder packing transitions with high packing  
16 densities and excessive deformations (bacteria deforms nearly twice its original length scales).  
17 In contrast, thin-film instability-led hole formation at the center of the droplet engenders spatial  
18 packing of bacteria analogous to honeycomb weathering. The varying physical forces acting  
19 on bacteria based on their respective spatial location inside the droplet cause an assorted  
20 magnitude of physical stress. Self-assembly favors the bacteria at the rim of the droplet, leading  
21 to enhanced viability and pathogenesis on the famously known “coffee ring” of the droplet  
22 compared to the bacteria present at the center of the droplet residue. Mechanistic insights  
23 gained via our study can have far-reaching implications for bacterial infection through droplets,  
24 e.g., through open wounds.

## 25 **Main**

26 Bacteria orchestrate robust collective responses in dynamic fluid environments by using  
27 different physical mechanisms (e.g., suppression of its transport due to fluid shear<sup>1</sup>, oscillatory  
28 rheotaxis<sup>2</sup>, swimming against the flow in the wake of curved surfaces/pillars leading to their  
29 attachment on the surfaces<sup>3</sup>) that have been developed by evolution over eons. Several recent  
30 studies have consolidated the notional importance of the interplay of physical forces in  
31 affecting the transport properties of bacteria, their colonization, and survival strategies in novel  
32 habitats<sup>4-8</sup>. Unlocking how rugged environments leads to an increase in fitness of the microbes  
33 may reveal the physical interactions that cause Anti-Microbial Resistance (AMR)<sup>9</sup>.

34 Opportunistic bacterial pathogens like *Klebsiella Pneumoniae* (KP) are known for their high  
35 frequency and diversity of AMR genes<sup>10-12</sup> and hence are chosen as a model organism in this  
36 study. Besides, bacteria spread through complex transmission routes, for example, through  
37 aerosols<sup>13</sup> and fomites<sup>14</sup>, and are subjected to various physical stresses in wild environments.

38 Bacteria inside droplets experience several physical stresses<sup>15</sup>, such as shear stress due to fluid  
39 motion in the environment, starvation stress (caused due to lack of nutrients), desiccation stress  
40 (caused due to depletion of water from bacterial cell wall due to evaporation), and stress due  
41 to harsh environmental conditions (fluctuating humidity and temperatures), to name a few. The  
42 bacteria-laden droplets in contact with any surface will eventually evaporate and lead to a  
43 drastic loss in viability of the bacteria<sup>16</sup> due to desiccation at the end stage of evaporation.  
44 However, despite fatal death due to desiccation, few bacteria continue to survive over weeks  
45 on inanimate dry surfaces<sup>17</sup>. Studies show that the final survival of bacteria or even virus in an  
46 evaporating droplet depends on its ability to withstand drying-induced stress<sup>18-20</sup>. The bacteria  
47 on the dried residue of droplets also form patterns, including “coffee rings”; however, motile  
48 bacteria can also alter the deposition patterns by evenly distributing the bacteria on the contact  
49 surface of the dried residue of the droplet<sup>21</sup>. The wettability of the bacterial surface/cell wall  
50 also plays a vital role in forming deposition patterns and the adhesion characteristics on the  
51 surface<sup>22,23</sup>. Order to disorder transition in the coffee ring deposit is observed in both spherical  
52 and rod-shaped inert particles<sup>24,25</sup>. The disordered region is characterized by a random packing  
53 pattern and dispersion in the Voronoi area<sup>26</sup>. However, it is unclear if an active matter like  
54 bacterial cells would exhibit a pattern and trend in packing at the coffee ring.

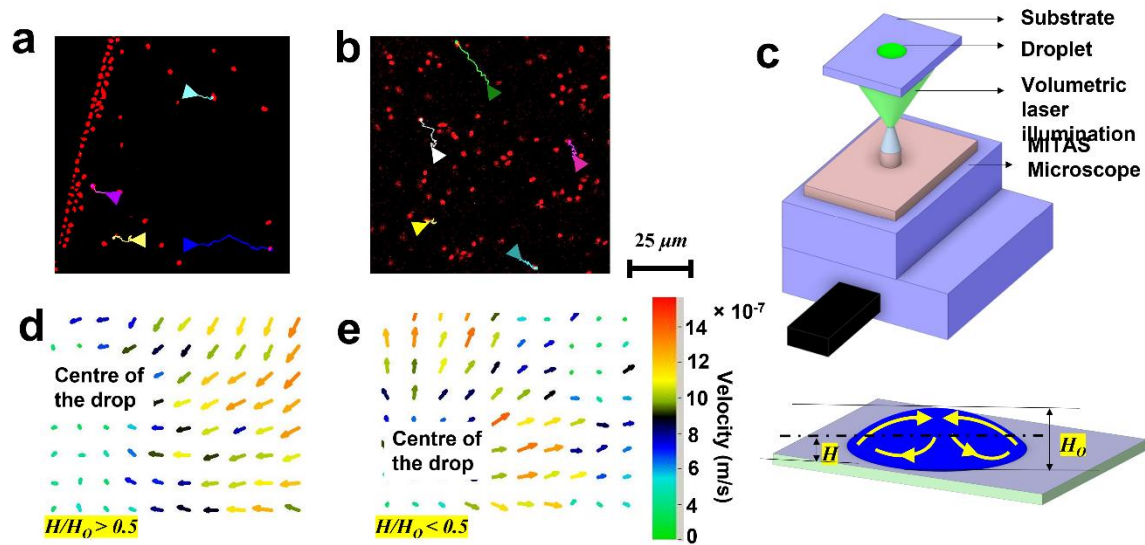
55 There are significantly fewer works on the effect of desiccation on the survivability of  
56 bacteria<sup>27-31</sup>. Even these works have only studied what happens to the overall viability without  
57 considering the fate of bacteria (i.e., its morpho-topological changes, the viability variation  
58 within different regions of the deposit, the effect of self-assembly). In the present work, we  
59 will explore how the physical mechanism of self-assembly of KP in evaporating droplets favors  
60 a few bacteria to survive the adverse condition. Investigating the complex patterns formed by  
61 the evaporating droplets containing bacteria that may enhance the survivability and  
62 pathogenesis of bacteria, in the present article, we study the physics pertaining to the self-  
63 assembly-based survivability mechanism of KP in evaporating sessile droplets.

#### 64 **A. Bacterial self-assembly in evaporating droplets**

65 Particle aggregation towards the contact line on pinned sessile droplets evaporating in an  
66 ambient environment is a well-known phenomenon<sup>32</sup>. The colloids suspended in the droplet  
67 are driven along with the flow created to replenish the evaporating water at the edge of the  
68 water droplet, resulting in a coffee ring-type deposition. In contrast, bacterial aggregation is  
69 much more complex than inert particles. For example, bacteria are soft/deformable, have semi-  
70 permeable cell walls, interact, form colonies/combined structures, etc. In addition, droplets  
71 containing bacterial suspension exhibit pinned contact line for the entire evaporation lifetime  
72 on hydrophilic substrates<sup>33-35</sup>.

73 In our experimental set-up, we placed a 1  $\mu$ l droplet of milliQ, suspended with the KP bacteria,  
74 on the clean glass surface, as shown in Fig. 1 (c) (refer to the “Droplet Evaporation” in the  
75 Methods Section for the detailed protocol). As observed from the live-cell imaging, most of  
76 the KP bacteria adsorb at the surface of the droplet (as represented in Fig. 2 (a)) due to the high  
77 electric charge on the bacterial surface (refer to Table 1 in the supplementary information).  
78 Several bacteria faithfully follow the flow inside the droplet, laterally stacking themselves at  
79 the droplet rim (see Video 1, Fig 2. (b)).

80 Although evaporation-driven flow (EDF) inside the droplet exists, all bacteria may often not  
81 faithfully follow the flow<sup>36</sup>. Live-cell imaging reveals the real-time transport of bacteria in the  
82 droplet near the glass surface (at a 10  $\mu$ m distance from the glass surface); Fig. 2 (a) and (b)  
83 show the path line followed by the individual bacteria. Several bacteria move towards the edge  
84 of the droplet; however, few move away from the edge (refer to Fig.1 (a) and Video 1). Few  
85 bacteria in the central region get adhered to the surface and wiggle there, while few others  
86 move in an arbitrary direction. Further, we study the flow inside the droplet to understand its  
87 role in the transport of KP in the droplet. The Micro-Particle Image ( $\mu$ -PIV) Velocimetry  
88 technique is used to quantify the flow inside the droplet, and the schematic representation of  
89 the experimental set-up is shown in Fig.1 (c) (refer to the Methods section for the details of the  
90  $\mu$ -PIV experiment).



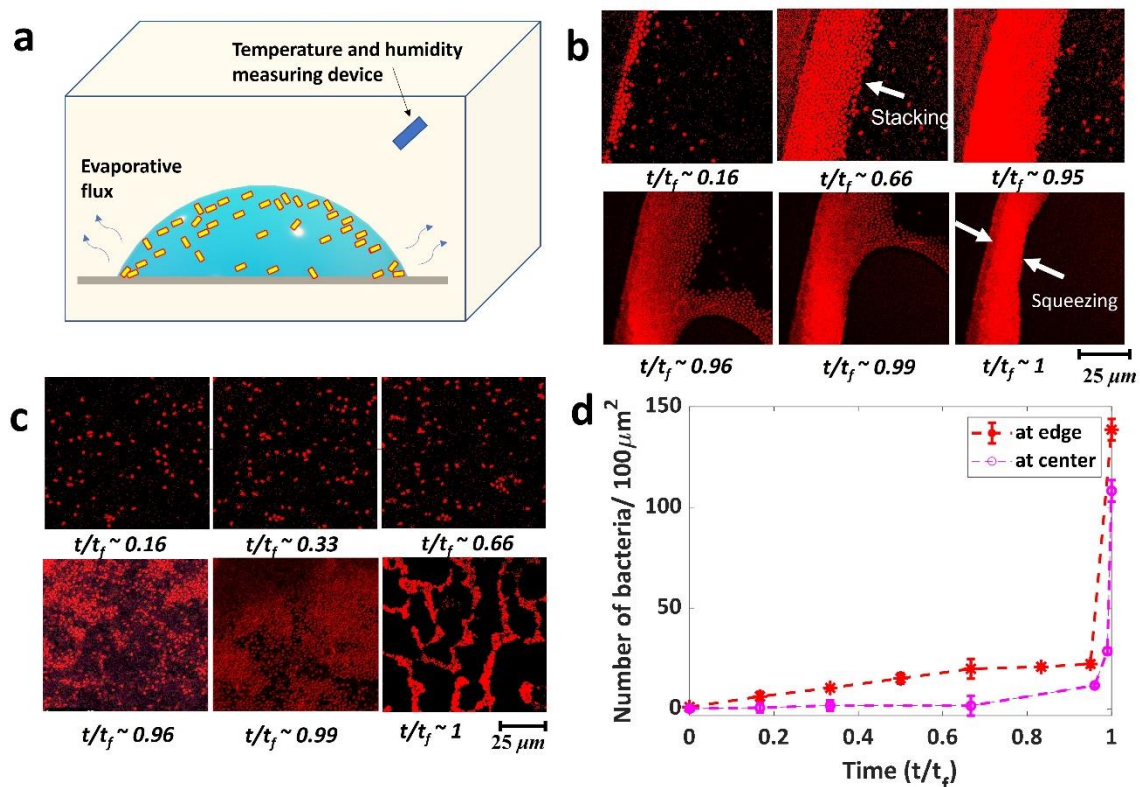
91

92 **Figure 1 Live Cell tracking of bacteria and hydrodynamics inside the droplet laden with**  
 93 **KP. Snapshot of live cell image of the KP suspension droplet (at  $t/t_{\sim} 0.1$ ) at the (a) edge**  
 94 **of the droplet, (b) center of the droplet. The colored arrows in (a) and (b) show the**  
 95 **direction of transport of KP, and the corresponding colored line is the path line followed**  
 96 **by the respective bacteria for 10 seconds. (c) Schematic representation of the  $\mu$ -PIV**  
 97 **experimental set-up. Vectors of velocity (d) at  $H/H_0 \sim 0.1$  (e) at  $H/H_0 \sim 0.6$ . The scale bar**  
 98 **for the velocity vectors for (d) and (e) is adjacent to (e).**

99 Our investigations show circulatory flow in the bacteria-laden Milli-Q water droplet. The flow  
 100 is radially inwards (i.e., towards the center of the drop), as shown in Fig.1 (d). Near the glass  
 101 surface, the flow is directed radially outwards (see Fig.1 (e)). Since the KP bacteria used in the  
 102 experiments are non-motile, the bacteria moving away from the edge of the droplet (in Fig.1  
 103 (a)) are, in reality, moving upwards along with the recirculatory flow inside the droplet. Near  
 104 the end of evaporation, the bacteria that has not settled in the coffee ring gets deposited in the  
 105 rim of the local dewetting hole front, as discussed in section C.

106 As shown in Fig. 2 (b), the ordered packing of KP is similar to the ordering of rod-shaped  
 107 particles previously observed by Dugyala et al.<sup>37</sup>. As the height of the droplet becomes thinner,  
 108 the evaporative flux at the contact line increases. Subsequently, the flow velocity inside the  
 109 droplet towards the contact line also increases. Studies have shown a rapid increase in velocity  
 110 near the end of evaporation, usually referred to as ‘the rush hour effect.’ The resulting  
 111 deposition at the coffee ring generally exhibits an order to disorder transition<sup>37–39</sup>. We observe  
 112 a similar order to disorder transition self-assembly in the case of KP bacteria.

113 The bacterial number density in a region is calculated by considering a region of interest in the  
 114 image (for a given instant) and subsequently counting the number of bacteria in the given  
 115 region. The values plotted in Fig.2 (d) are the averages of bacterial count in six arbitrary regions  
 116 at any given instants, and the error bar corresponds to the standard deviations of the same. This  
 117 is scaled/ $100 \mu\text{m}^2$  in order to have a substantial number of bacteria for a given region. However,  
 118 in the end stage of evaporation ( $t/t_f = 1$ , where  $t$  is the image at any given time instant and  $t_f$  is  
 119 the total time of evaporation of the droplet), the bacteria is squeezed and very closely packed  
 120 such that it is not possible to obtain the bacterial count in the given region from the live-cell  
 121 image. Hence, the bacterial count at  $t/t_f = 1$  is calculated from the Scanning Electron Microscopy  
 122 (SEM) images (See Fig.S1 in the supplementary information). It is observed that the bacterial  
 123 number density in a given region at the droplet rim increases drastically with time, leading to  
 124 very close packing of the bacteria (refer to Fig. 2 (b) and (d)). At the center of the drop, we see  
 125 a sudden increase in the visible number of bacteria during the end stages of evaporation. The  
 126 focus is adjusted to visualize a section plane of a droplet near the substrate (at a plane  $10 \mu\text{m}$   
 127 from the glass surface). Since many bacteria reside near the air-water interface of the drop, as  
 128 the drop height reduces, the bacteria move along with the open surface of the droplet towards  
 129 the substrate and thus become visible in the live-cell imaging in the end stage of evaporation.



131 **Figure 2 Spatio-temporal dynamics of self-assembly of *Klebsiella Pneumoniae* (KP) in**  
132 **evaporating droplets. (a) Schematic of an evaporating droplet containing the KP bacteria**  
133 **in controlled atmospheric conditions. Temporal sequential live-cell images of KP**  
134 **deposition near the glass surface (at a plane 10  $\mu\text{m}$  from the surface), (b) at the edge, (c)**  
135 **at the center of the droplet. (d) Bacterial count scaled/ $100 \mu\text{m}^2$ . For time  $t/t_f=1$ , the**  
136 **bacterial number is counted from the SEM images (as the individual bacteria is not**  
137 **distinguishable in the fluorescence images).**

138 The thin film of liquid and bacteria residue at the end stage of the evaporation of the droplet  
139 ( $t/t_f \sim 0.99$ ) undergoes instability; subsequently, capillary forces dominate, leading to the  
140 formation of holes and compact packing of KP as shown in Fig.2 (c). The bacterial number  
141 density at the center of the droplet residue (for  $t/t_f=1$ ) is calculated from the SEM images in the  
142 region where the bacteria aggregates disregarding the region of holes (see Fig.2 (c)). Fig. 2(d)  
143 shows that the compaction of KP happens in the last one percent of the total evaporation times,  
144 and the self-assembly is dominantly the result of capillary forces and thin-film instabilities at  
145 the end stage of evaporation. This phenomenon in the case of KP is explained in sections C  
146 and D.

147 <sup>36</sup>

## 148 **B. Ordered to dis-ordered transitions and simultaneous squeezing and buckling of** 149 **bacteria on “coffee ring”**

150 Based on the type of self-assembly, we have classified the regions within the droplet residue  
151 into three types: 1) ordered region near the edge of the droplet residue – referred to as “Outer  
152 Edge” as shown in Fig.3 (a) and (b). 2) the disordered region – referred to as the “Inner edge”  
153 as shown in Fig.3 (a) and (b). 3) the central region of residue – is referred to as “honeycomb  
154 weathering” Fig.5(a). An aerial view of the bacterial deposits captured from SEM has been  
155 used to analyze the size and bacterial ordering. The bacteria profile is manually marked using  
156 a digital pen to precisely detect the bacterial edges while processing the image (Fig.3 (g)).  
157 ImageJ software is used to binarise the image, and the ‘analyze particle’ plugin is used to get  
158 the size and position characteristics.

159 We define the maximum and minimum ferret length ratio as the aspect ratio (ratio of length  
160 (L) to the width of the bacteria (W)) of the bacteria. Aspect ratio and vertical height are higher  
161 for the bacteria that got squeezed laterally. The Aspect ratio of bacteria is averaged radially  
162 from the edge (see Fig.3 (b)). The radial distance from the edge, R, is normalized with the

163 thickness of edge deposition (the coffee ring thickness),  $R_e$ . Three different deposits have been  
164 used to get the statistical mean of the plot shown in Fig 3 (c). The deposits from separately  
165 grown cultures have also been tested to ensure repeatability. The aspect ratio is higher at the  
166 outermost edge than in the central region for all the cases. The aspect ratio is highest at  $R/R_e$   
167 between 0.35 to 0.5. Bacteria in this region are highly jammed between the bacteria that settled  
168 at the outermost edge and the incoming bacteria during the rush hour and squeezing effect, as  
169 discussed earlier. The bacteria in the inner edge are in a wide range of aspect ratios depending  
170 on the configuration of the bacteria. Bacteria at the inner edge may be folded due to excessive  
171 desiccation stress and attain U shape<sup>40</sup>.

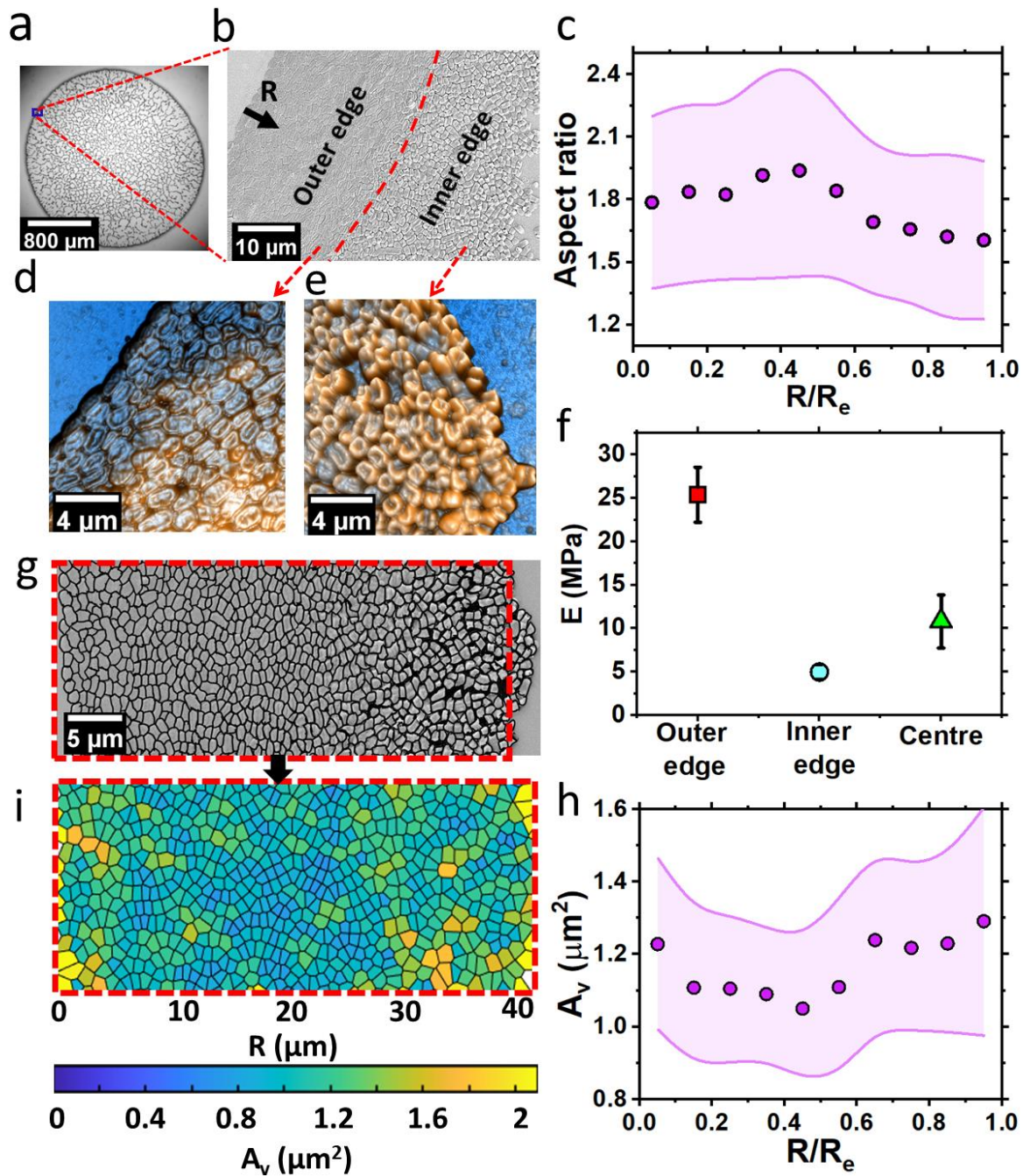
172 Atomic force microscopy, AFM image (Fig. 3 (d) & (e)) confirms this observation and gives a  
173 clear picture of the bacterial morphology at the inner and the outer edge. The bacteria at the  
174 outer edge are packed with their major axis along the periphery, whereas the bacteria at the  
175 inner edge exhibit a random arrangement. Marin et.al<sup>24</sup>. observed order to disorder transition  
176 in inert sphere particles, and Dugyala<sup>37</sup>et.al<sup>25</sup>. observed this in colloidal rods. The thickness of  
177 the bacterial deposits at the edge varies from 300 nm at the outermost edge up to 700nm in the  
178 highly squeezed region. At the same time, the folded bacteria at the inner edge showed a height  
179 in the range of 350 to 500 nm. Height variation in the outer edge can occur because of variation  
180 in squeezing and water content in bacteria due to variation in the level of desiccation. Whereas  
181 in the inner edge, this variation is due to the degree of folding up of the bacteria, the bacteria  
182 that have folded up more show higher height. Folding of bacteria is a preventive measure to  
183 avoid desiccation. The bacteria try to reduce the exposed area for desiccation by attaining a  
184 coccoidal shape<sup>40</sup>. The bacteria at the inner edge folds because the lateral surfaces are also  
185 exposed for desiccation, unlike the bacteria at the outer edge region enclosed by the closely  
186 packed adjacent bacteria hindering evaporation from its lateral sides. The bacteria at the outer  
187 edge are closely packed, so they are constrained to fold up like those in the disordered region.  
188 Folding is neither seen in the outermost first line of the bacteria on which one of the lateral  
189 surfaces is exposed to the ambient. We hypothesize that the bacterial cell-substrate bonding  
190 might be higher here due to prolonged cell-substrate interaction, which would have prevented  
191 cell folding in the lateral direction.

192 The force-distance spectroscopy analysis done on the bacterial samples through nano  
193 indentation (refer to methods section for details) at various regions in the deposit reveals the  
194 elasticity of the cell membrane of the bacteria. The Modulus of Elasticity (E) of the bacterial  
195 membrane is obtained using the Oliver Pharr model. The results show that the outer edge

196 bacteria are stiffer than the other bacteria. The squeezing effect on these bacteria leading to  
197 very close packing, has increased the stiffness (see Fig. 3 (f)) by nearly one order. E of the  
198 bacteria is  $25 \pm 3$  MPa,  $5 \pm 1$  MPa, and  $11 \pm 3$  MPa at the outer edge, inner edge, and central  
199 region, respectively. The variation in the elasticity modulus can be attributed to the level of  
200 desiccation and ordering dynamics induced gap between the bacteria based on the location.

201 In addition, the difference in the cross-sectional area normal to the indentation direction would  
202 also be a factor as the bacteria is twice as stiffer in the circumferential direction than in the  
203 axial direction.<sup>41</sup> Deng et al. showed that axial Modulus  $E = 23 \pm 8$  MPa, is less than half the  
204 circumferential Modulus  $E = 49 \pm 20$  MPa. In the current study, we obtained the elasticity  
205 modulus of the exposed top surface by AFM cantilever tip indentation for all cases. In the case  
206 of outer bacteria lying with their axial direction along the periphery of the droplet deposit, the  
207 top surface indentation gives the circumferential Modulus. The bacterial cross-section in the  
208 axial direction is lesser than in the circumferential direction, and such is





209

210 **Figure 3 Bacterial Self-Assembly at the edge of the droplet.** (a) Optical image of the dried  
 211 residue of the KP droplet. (b) SEM micrograph of the KP deposition at the edge/rim of  
 212 the deposit. (c) The plot of the radially averaged aspect ratio of the bacteria as seen from  
 213 the top view vs. the normalized distance ( $R/R_e$ ) from the outer edge. Where  $R$  is the radial  
 214 distance from the edge of the contact line, and  $R_e$  is the thickness of edge deposition.  
 215 Atomic force microscopy images at the (d) outer edge and the (e) inner edge of the  
 216 precipitate as shown in (b). (f) The plot of the Modulus of Elasticity values ( $E$ ) for bacteria  
 217 at the outer edge, inner edge, and center. (g) SEM micrograph on the edge of the deposit,  
 218 bacteria marked with black border for centroidal Voronoi tessellation processing. (i)

219 **Voronoi cells of the corresponding bacterium shown in. g) color marked according to**  
220 **their size. (h) The Voronoi area of the bacterial deposits was averaged and plotted with**  
221 **normalized distance from the edge  $R/R_e$ .**

222 the elasticity modulus. The inner edge bacterial cross-section gets reduced by folding up, which  
223 decreases elasticity modulus. Correspondingly, we hypothesize, that the bacteria with less  
224 water content is less stiff and deforms more at a given force during indentation. The reasoning  
225 is further supported by the maximum unbinding force (force required to detach the AFM probe  
226 from the sample during retraction) on the indenting probe shown in Fig.S2. The bacteria  
227 deposited at the outer edge show the highest unbinding force (adhesion force) compared to the  
228 bacteria at the other sites. Bacterial cells secrete protein across their membranes upon contact  
229 with other surfaces<sup>42,43</sup>. The variation in adhesion force on the bacterial surface can be attributed  
230 to the secretions from bacterial cells upon interaction with the substrate. Bacterial cells at the  
231 outer edge are in close proximity with the substrate for a longer duration before desiccation,  
232 whereas the bacterium at the central regions gets deposited much later. Shear stress imposed  
233 on the bacteria in different regions could also be an essential factor in expressing adhesive  
234 substances through its membrane which inturn reduces desiccation.

235 The centroidal positions of each bacterium obtained through image analysis are used to study  
236 the bacterial ordering. The bacterial ordering is analyzed by centroidal Voronoi tessellation  
237 using MATLAB. The Voronoi cells in Fig. 3 (i) show the Voronoi area ( $A_v$ ) varying from 0.5  
238  $\mu\text{m}^2$  to 1.85  $\mu\text{m}^2$ . The Voronoi area of the cells is obtained by processing the SEM image  
239 Fig.3(g), where the bacterial profile is marked manually for discrete identification of cells. The  
240 average Voronoi area is 1.1  $\mu\text{m}^2$  at the outer edge and 1.21  $\mu\text{m}^2$  at the inner edge. The Voronoi  
241 area reduces inwards in the outer edge region where the bacterium is more squeezed. In  
242 comparison, the Voronoi area increases towards the disordered region. For inert non-  
243 deformable particles, it is observed that the Voronoi area shows a dispersion (sudden increase  
244 in the Voronoi area) from the order to the disordered region<sup>24</sup>. Evidently, such dispersion is not  
245 observed in the bacterial deposition. There could be three causes for this: the squeezing effect  
246 during the hole growth, the capillary force leading to packing during the evaporation of the  
247 mesoscopic thin layer, and the folding of the bacteria.

248 The supplementary Figure ( Fig.S2) shows the overall picture of bacterial deposition at the  
249 edge. The deposit thickness increases from the outer edge and reaches a maximum at  $R/R_e$  of  
250 around 0.4 to 0.5. There is a strong relation between the increase in thickness, the decrease in

251 the Voronoi area, and the increase in aspect ratio. The squeezing effect leads to morphological  
252 changes in the bacterial cells resulting in the increment in height and reduction in the area of  
253 contact with the substrate to conserve the volume. Moreover, due to lesser exposed surface area  
254 and desiccation, these bacteria would have more water content and have higher volume than  
255 the edge bacteria and the ones with a gap between them (inner edge). The height variation of  
256 bacterial deposits in the central regions remains less the same, around 200-300 nm(Fig.S3) at  
257 a different location depending on the local ordering of bacteria.

### 258 **C. Thin-film instability leading to honeycomb weathering**

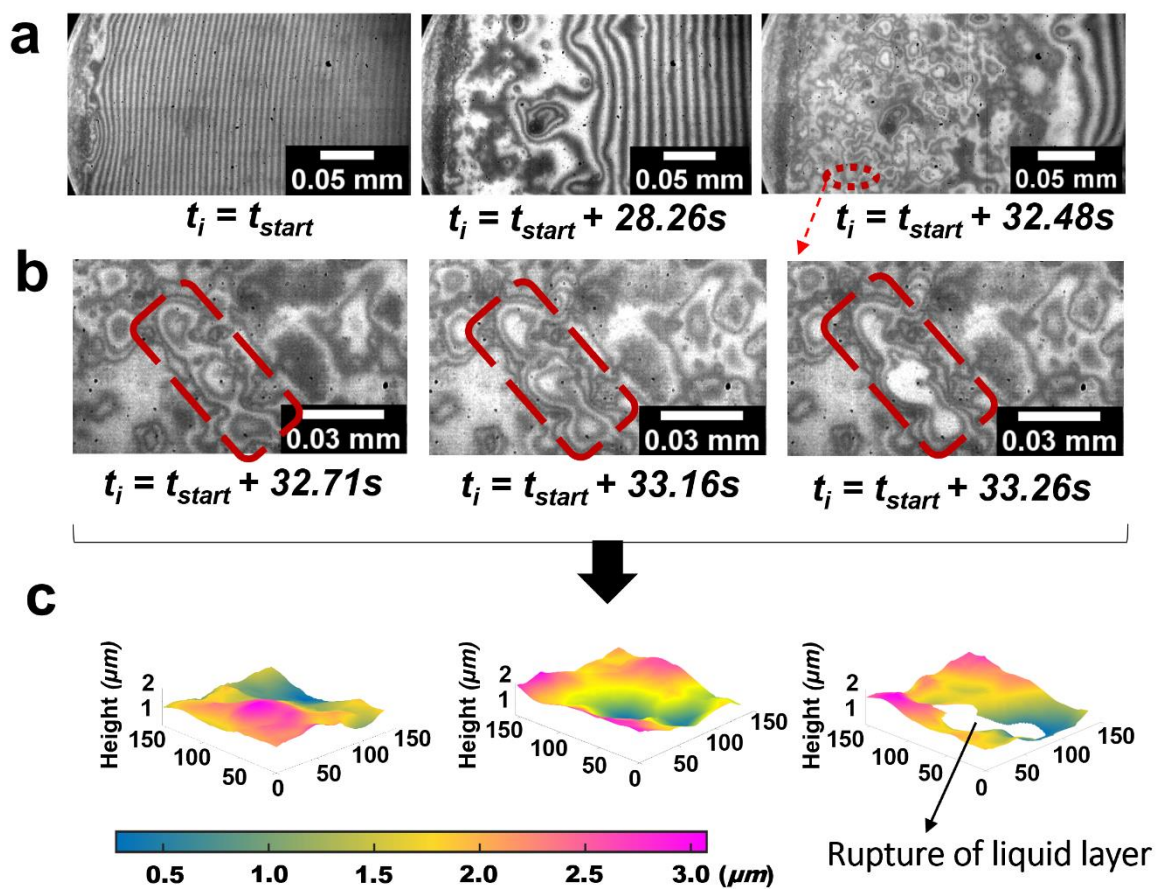
259 Not all bacteria in the droplet get settled at the ring. Depending on the concentration, interface,  
260 and evaporation dynamics, a significant proportion of bacteria would remain dispersed in the  
261 liquid film. In the current study about 50 to 60 % of the bacteria gets deposited on the edge and  
262 the thickness varies from 38 to 44 nm. Liquid thin-film dynamics determine the final deposition  
263 of bacteria not settled in the coffee ring. The perturbations in the liquid thin film would cause  
264 rupture, hole growth, and resulting island formation<sup>44</sup>. The size and shape of these islands  
265 depend on the liquid properties and size, shape, and interfacial properties of the colloids. The  
266 bacteria come closer, leaving a region of low liquid film thickness where the rupture would  
267 occur.<sup>45-47</sup>.

268 The deposition of bacteria in the central regions follows a sequence of events discussed in this  
269 section. At shallow film thickness, the contact line de-pins, leaving a fine mesoscopic layer of  
270 thin liquid film containing bacteria distributed throughout. The depinning is followed by the  
271 thin film instability leading to the cellular pattern formation. Due to thin-film capillary  
272 instability, the liquid film thickness varies along the wetted area. These perturbations get  
273 enhanced due to the presence of bacteria. Fringe patterns were observed as shown in Fig 4 a)  
274 through the reflection interference microscopy at low film thickness. Figure 4 shows the thin-  
275 film variation of the bacteria-laden droplet at various time instants and the phenomena of the  
276 dewetting process of the liquid layer at the conclusive phase of evaporation. Here we take  $t_{\text{start}}$   
277 as the time when depinning has started and  $t_i$  is the instantaneous time which is  $t_{\text{start}}$  when  
278 depinning has initiated. At the initial time instants ( $t_i = t_{\text{start}} + 3.28\text{s}$ ), densely spaced fringe  
279 patterns were formed in the form of dark and bright bands, as seen in Fig.4 (a). These patterns  
280 signify the presence of a thicker liquid layer, and from the initial observance of the fringes, the  
281 contact angle of the liquid layer is estimated at approximately  $\approx 5.6^\circ$ . As time progresses, the  
282 fringe width evolves to wider patterns, and instigation of circular patterns of the liquid layer is

283 evident nearer to the contact line of the droplet. The formation of multiple circular patterns in  
284 the liquid layer for ( $t_i \approx t_{start} + 29.20$ ) represents the thinning of the liquid layer compared to  
285 the initial time instants that result in a reduction in thickness of the thin film. The observance  
286 of multiple circular rolls is slightly distant from the leading edge. This phenomenon is  
287 predominant due to the deposition of more bacteria along the droplet's edge.

288 The pinning of droplet without receding the liquid layer consents to the existence of the thin  
289 film. Once the thickness of the thin film is reduced, the evaporation of the liquid layer  
290 surrounding the bacteria elucidates the variation in thickness resulting in the formation of  
291 multiple roll structures and the onset of the dewetting process of the liquid layer. The rupture  
292 of the thin film and the sequence of variation in thickness of the liquid layer at the selected  
293 regions of the initial de-wetting process are presented in Figs 4 (b) and (c). The formation of  
294 multiple rolls at a specific time of 29.43s and adjoining of the rolls in the course time till

295



296

297 **Figure 4 Thin film instability at the center of the droplet. (a) The liquid layer at varying**

298 **time instants during evaporation of the droplet (b) Insights of the de-wetting process in**  
299 **the thin-film layer (c) Variation of the thickness profiles along with the de-wetting**  
300 **phenomena.**

301 the rupture of the thin film is evident from Fig. 4 (b). The rupture of the liquid layer is observed  
302 from the interferometric images at  $t_i = t_{\text{start}} + 29.98\text{s}$ . The associated two-dimensional  
303 distribution of the height profiles and variation of the thin film was presented in Fig. 4 (c).  
304 During the  $t = 29.43\text{s}$ , the presence of multiple rolls (in the selected yellow regions) shows the  
305 increase in the height of the thickness profile, nearly having the maximum height of  $3\ \mu\text{m}$ .  
306 In contrast, the adjoining regions of the rolls represent the reduction in thickness variation  
307 nearly to  $1\ \mu\text{m}$ . Similarly, at  $t_i = t_{\text{start}} + 29.98\text{s}$ , the distribution of the height profile surrounding  
308 the rupture region of the liquid layer varied from  $0.5$  to  $1.5\ \mu\text{m}$  as the liquid layer recedes to  
309 the adjacent regions. Therefore, the formation of multiple roll-structures (as in  $t_i = t_{\text{start}} + 29.20$ )  
310 leads to multiple de-wetting locations regions in the fluid layer, leading to multiple streaks  
311 during the droplet's evaporation (deposition of bacteria) from the droplet edge to the center of  
312 the droplet. Since the droplet de-pining initiates from the edge, the hole formation starts from  
313 the edge. The hole formation progress towards the central region as the film thickness  
314 decreases, as shown in Fig. 5 (a). While the hole near the droplet edge keeps growing, another  
315 hole forms adjacent to the droplet center. The growing front from two holes merges, creating  
316 an island of bacteria.

317 Due to perturbations on the thin film, the hole formations will either increase the surface energy  
318 or decrease it. For a negative change in energy, the hole continues to grow, and for a positive  
319 change in energy, the hole shrinks. Using the energy minimization criterion for a quasi-static  
320 system of hole radius  $r_0$  and inner hole distance  $D$ , the change in energy of a perturbed system  
321  $\Delta E$  can be given as<sup>44</sup>,

$$322 \quad \Delta E = \pi h_{\text{film}}^2 \sigma_v \cdot \left[ \frac{-4}{(3+4\ln\rho-4\rho^2+\rho^4)} - \beta\rho^2 \right],$$

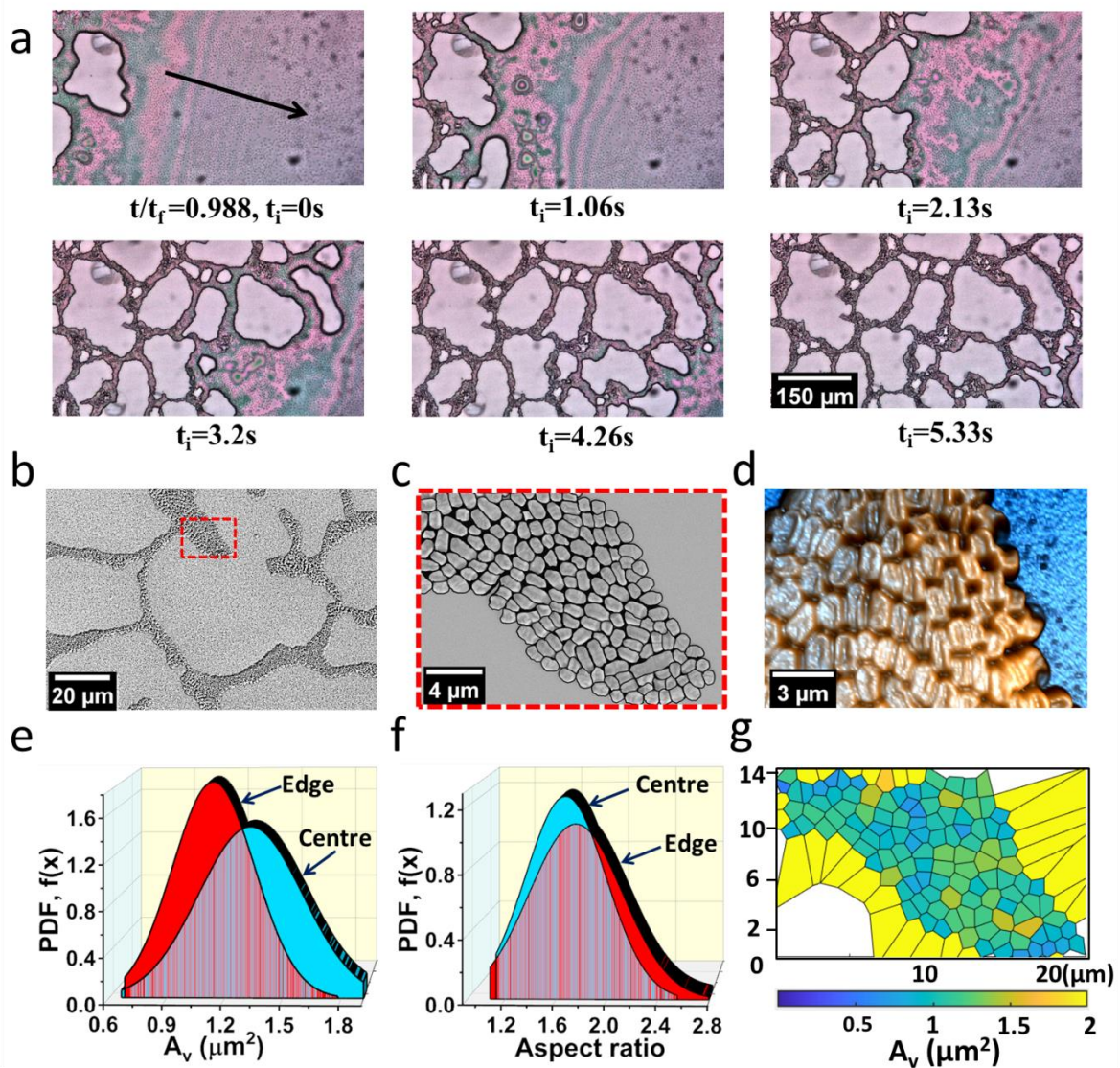
$$323 \quad \text{Where, } \beta = \left( \frac{R}{h_{\text{film}}} \right)^2 \cdot (1 + \sigma_s/\sigma_v), \quad \rho = r_0 / D$$

324 For  $\beta < 19.5$ , holes of any size will shrink, and the film will become flat. At  $\beta > 500$ , holes will  
325 grow for most of the range of  $\rho$ . Infinitesimally small holes will shrink at any value of  $\beta$ .  $\sigma_v$   
326 represents the film-vapor surface energy  $\sigma_s$ , is the film-substrate surface energy. The major  
327 players in determining the energy change are the hole size, inter-hole distance, and film

328 thickness. At high film thickness, smaller holes produce a positive change in energy, resulting  
329 in shrinking while larger holes could grow. At a film thickness of order  $10\ \mu\text{m}$ , holes of size  
330  $r_0 > 3.2\ \mu\text{m}$  will create a negative change in surface energy and start to grow in the current case.

331 The instantaneous hole growth at the edge and the central region is compared in Fig.S4 The  
332 pinned contact line, and the edge deposits impede the growth of holes near the coffee ring. The  
333 bacterial cell assembly at the edge is squeezed by the growth of holes adjacent to it. The cells  
334 cannot move further due to the pinning of the contact line. Thus, the hole growth is restricted  
335 toward the coffee ring. However, the holes can still grow towards the center of the droplet. The  
336 normalized hole area exhibits a linear variation in Fig.S4.

337



338

339 **Figure 5 Bacterial Self-Assembly at the central region of the droplet. (a) Spatio-temporal**  
340 **evolution of the liquid film leading to the rupture and hole growth resembling a cellular**  
341 **pattern (b) SEM micrograph of a cellular structure at the central region (c) Zoomed in**  
342 **SEM micrograph with marked bacterial edge profile, represent the bacterial ordering in**  
343 **the cellular structure (d) AFM image shows the deposited bacterial morphology and self-**  
344 **assembly at the central region (e) Plot comparing the Voronoi Area at the central region**  
345 **to that of the edge of the deposit through Probability density function, PDF, f(x) plot (f)**  
346 **plot of PDF of aspect ratio (viewed normal to the substrate) of bacteria at the edge and**  
347 **center (g) Color-marked Voronoi cells of the bacterial deposits corresponding to (c).**

348 The holes formed at a location further away from the edge can grow with lesser restriction  
349 initially. As the adjacent holes start to impinge on each other, growth is slowed down. The  
350 normalized hole area variation in the central regions fits very closely to the logarithmic curve  
351 (Fig.S3). Here, the growth rate reduces exponentially with time, which shows that the dominant  
352 mode in the hole growth mechanism is the surface diffusion<sup>44</sup>. Whereas for the holes near the  
353 coffee ring, the growth rate is nearly the same as dictated by the evaporation kinetics<sup>44</sup>. The  
354 hole growth rate for an evaporation dominated case is,  $\dot{\rho} = \tan\theta \cdot \frac{A}{h_{film}}$  Where  $\theta$  is the  
355 equilibrium wetting angle, A is the gas-phase transport coefficient, defined as,  
356  $p_o \cdot \sigma \cdot \frac{\Omega^2}{(2\pi M)^{\frac{1}{2}}(kT)^{3/2}}$ ,  $p_o$  is the equilibrium vapour pressure on the film surface,  $\sigma$  is the surface  
357 energy per unit area of the film/vapour interface,  $\Omega$  is the atomic volume, M is the atomic  
358 weight, and kT is the thermal energy.  $\dot{\rho} \sim 1\mu m/s$  which is of the same order as the growth rate  
359 observed in the experiments for the holes. The holes at the central region have an initial velocity  
360 two orders higher than that calculated, which drastically reduces to the order of  $1\mu m/s$  in less  
361 than half the growing time. The total growing time, shape, and size of holes vary randomly.  
362 The position of the hole inception, the inter-hole distance, and bacterial density distribution  
363 around the hole are the significant factors influencing the final hole size and shape, along with  
364 the fluid properties.

365 Habibi et al.<sup>48</sup> studied the pattern of particles in dewetting thin films and proposed a simple  
366 model for predicting the dewetting velocity,

367 
$$U_{Dewetting} \sim \frac{\sigma}{3\eta} \left(\frac{L_c}{w}\right)^2$$

368 Where  $\sigma$  is the surface tension of the liquid film,  $\eta$  is the effective viscosity of the thin liquid  
369 film,  $w$  is the characteristic size of the hole, and  $L_c$  is the bacterial size. The effective viscosity  
370 of the liquid film is a strong function of the volume fraction of bacteria. The Krieger–Dougherty  
371 type law for effective viscosity is  $\eta = \eta_0 (1 - \phi/0.466)^{-2.6}$ , where  $\phi$  is the volume fraction and  $\eta_0 =$   
372  $10^{-3}$  Pa.s. The equation gives very close values to the effective viscosity calculated using the  
373 above-given formula for dewetting speed<sup>48</sup>. For the wetting velocity of order  $10^{-5}$  m/s and  $10^{-6}$   
374 m/s, the effective viscosity of the medium is 0.0236 Pa.s. and 0.236 Pa.s, respectively. The  
375 corresponding bacterial volume fraction during dewetting is between 0.33 and 0.4. However,  
376 for bacteria, the curve fitting coefficients for calculating effective viscosity would vary, and  
377 there are no studies on the effective viscosity of bacterial solutions at volume fractions more  
378 than 0.1.

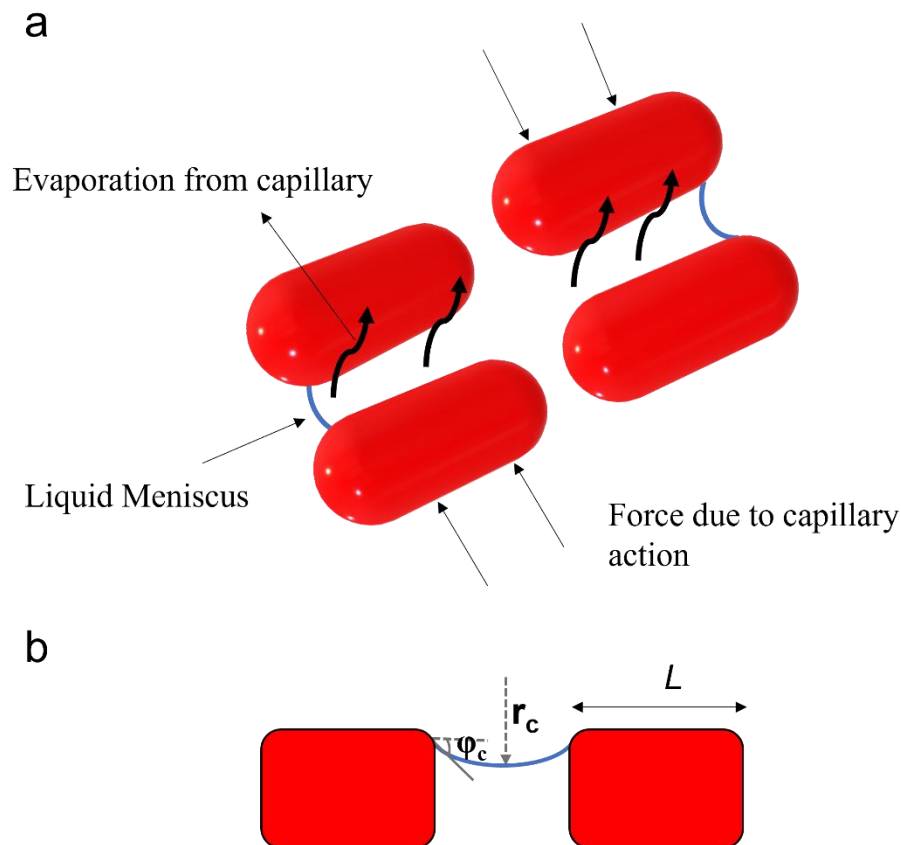
379 As shown in Fig. 5 (c), the SEM images are used to analyze the bacterial size and packing. The  
380 AFM image shows that the gap between the bacteria in the central regions is more than that at  
381 the edge. As a result, the Voronoi area of the bacteria aggregates in the central regions is higher  
382 than the edge bacteria aggregates, as shown in Fig. 5 (e). The variation in aspect ratio is nearly  
383 the same for the central and the edge regions. Since the bacteria in the central regions are also  
384 getting squeezed during the hole merging. However, the gap between the bacteria is the cause  
385 of a higher level of desiccation. The bacteria at the rim of the cellular deposits are also folded  
386 like the ones in the inner edges shown in Fig. 5 (d).

#### 387 **D. Mechanistic insights**

388 Along with the dewetting forces, the capillary forces due to the decaying liquid meniscus  
389 between bacteria make the bacteria move closer. Capillary forces led colloidal particle  
390 structuring in thin films is studied by Denkov and Kralchevsky et al.<sup>45,49</sup>. When the liquid film  
391 thickness decreases below the bacterial length scale, the drag force due to liquid flow decreases;  
392 microscopic video (Video 2) shows minimal bacterial movement. During the cellular pattern  
393 formation, the movement of the bacteria is driven by the capillary forces due to varying  
394 meniscus across the bacteria. In partially immersed particles, the deformation of the liquid  
395 meniscus gives rise to interparticle attraction or repulsion. The shape of the liquid meniscus  
396 between the bacteria and the surrounding region determines if the bacteria come closer or are  
397 moving apart. Capillary forces arise due to the pressure and surface effects at the three-phase  
398 contact line inclined at the particle surface. The capillary force of attraction is given by  $F_r = 2\pi$   
399  $\sigma r_c^2 (\sin^2 \phi_c) (1/L)$  for  $r_c \ll L \ll (\sigma/(\Delta\rho)g)^{1/2}$ , where  $r_c$  is the radius of the three-phase contact



400 line at the bacterial surface,  $\phi_c$  is mean meniscus slope angle at the contact line,  $\sigma$  is the surface  
401 tension of the liquid film and  $\alpha$  is the contact angle of the bacteria. The distance  $L$  between the  
402 bacteria can be determined by the Laplace equation of capillarity as  $L$  is the length scale of  
403 bacteria.. The capillary force between the bacteria is of the order  $10^{-4}$  N to  $10^{-6}$  N, depending  
404 on the distance between the bacteria.



405

406 **Figure 6 Mechanistic insights on bacterial aggregation. Schematic representation of (a)**  
407 **formation of a meniscus leading to the capillary attraction between the bacteria at the**  
408 **end stage of evaporation, (b) Side view of the liquid meniscus in between the bacteria**

409 In the central regions, the bacteria do not initially settle down on the substrate because both the  
410 substrate and bacteria are negatively charged (electrostatic repulsion). So, the monolayer of  
411 bacteria would start to form when the thickness of the liquid layer is equal to the size of the  
412 bacteria. The immersion capillary forces between partially immersed bacteria are much higher  
413 than the floatation capillary forces. Thus, the varying meniscus across the bacteria in the film  
414 results in a downward capillary force on the bacteria. At a later stage, the evaporating liquid  
415 between the bacteria alters the liquid meniscus creating an attractive force bringing the bacteria

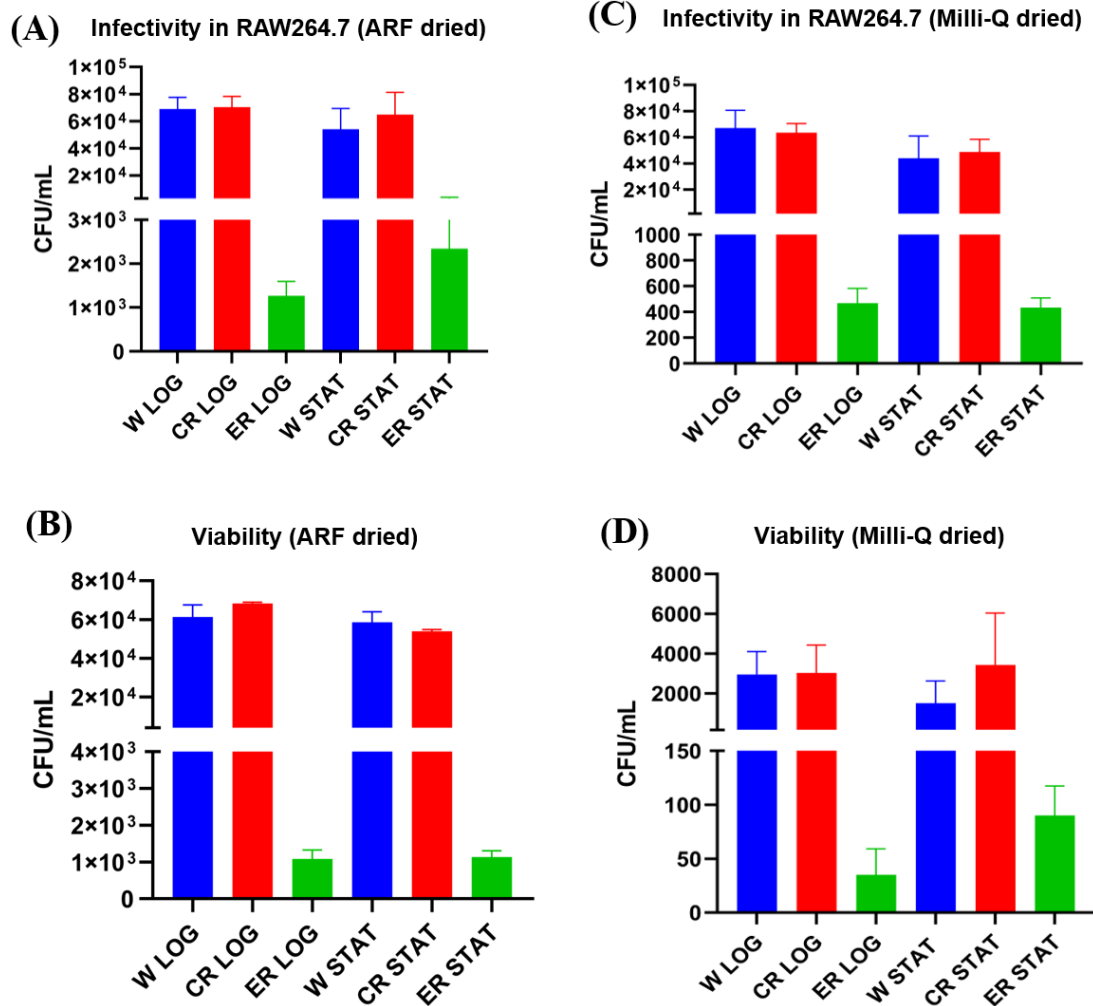
416 together. For the case studied, only a monolayer of deposits has formed. At a higher bacterial  
417 concentration and slower evaporation rate, bilayer and trilayer deposits could form.

418 Fig. S4(a) shows a monolayer deposit of bacteria in the central regions. Malla et al.<sup>50</sup> studied  
419 the effect of particle concentration and particle size on the edge deposition profile. The edge  
420 deposition is either a discontinuous or a continuous monolayer depending on the size of the  
421 particle, for very low particle concentrations below 0.1% v/v and diameter above 1  $\mu\text{m}$ . For  
422 very low bacterial concentrations of less than 0.1% v/v and an effective diameter of more than  
423 1  $\mu\text{m}$  used in this study it is reasonable to obtain a monolayer deposition at the edge. However,  
424 the variation in the thickness (Fig. 4(b)) of the deposition can be attributed to varying levels of  
425 desiccation within the edge deposition and the squeezing.

426

#### 427 **E. Bacterial survivability and pathogenesis aftermath desiccation of the droplet**

428 We studied the survivability and infectivity of bacteria suspended in both Milli-Q water and  
429 surrogate respiratory fluid (SRF). Milli-Q water is used to have a clear visualization of bacteria  
430 which is inhibited in the presence of other colloids such as mucin in real biofluids. To compare  
431 the viability of bacteria in different regions, we scrapped the deposits at the edge keeping only  
432 the central deposits and vice versa. The dried droplet deposits, either whole droplet (W), edge  
433 removed (ER), or center removed (CR), are used for the viability and infectivity studies (refer  
434 to Fig.S5). We observed that the bacterial survival KP was higher in the edge (of the droplet)  
435 deposited bacteria compared to center deposited bacteria, both in the case of bacteria  
436 resuspended in Milli-Q water or SRF. We also observed that the infectivity of the bacterium  
437 deposited at the edge is significantly higher than the center deposited bacteria. This could be  
438 primarily due to the upregulation of virulence genes upon enormous force exerted on the  
439 bacteria during the drying process<sup>51</sup>. We observe these similar observations for both SRF dried  
440 droplet and milliQ dried droplet, suggesting a possible role of physical force on the heightened  
441 virulence of the bacterium.



442

443 **Figure 7 Bacterial survivability and pathogenesis. (A) Infectivity of the bacteria dried in**  
444 **surrogate respiratory fluid (SRF) droplet in murine macrophages RAW264.7 cells. (B)**  
445 **Viability of bacteria dried in SRF droplet. (B) Infectivity of the bacteria dried in Milli-Q**  
446 **water droplet in murine macrophages RAW264.7 cells. (B) Viability of bacteria dried in**  
447 **Milli-Q water droplet. All experiments are repeated independently three times (N=3);**  
448 **error bars in the plot correspond to the standard error of the mean.**

## 449 F. Conclusions

450 The paper compares the nature of bacterial self-assembly, morphology, and viability in drying  
451 droplets. The bacterial cells generally die by desiccation. Studies<sup>29,31</sup> have reported that  
452 desiccation is an important mechanism by which the bacterial cells in the drying sessile droplet  
453 die. This study shows that the self-assembly and desiccation of bacteria suspended in a drying  
454 droplet significantly alter the morphology of the bacteria. The bacteria packed closely  
455 experience lesser desiccation as their exposed area to the ambient is less. The above discussion

456 serves as the reason why the bacterium at the edge is more viable than that at the central regions.  
457 In real biofluids and saline drying droplets, the increase in salt concentration causes osmotic  
458 shock, driving out water from the bacteria and resulting in death. In contrast, in a hypotonic  
459 solution like pure water used in this study, lysis could cause death. (by water intake and  
460 bursting). If bacteria survive the lytic process, water intake will help sustain the desiccation  
461 process longer than normal bacteria. A typical cellular pattern is formed by bacterial  
462 aggregation in the central region. The thin film instability led to the rupture of the liquid film  
463 causes, hole formation, and growth driving bacteria to come together and form cellular patterns.  
464 However, the gap between the bacteria is more in the central region, and the exposed area for  
465 desiccation is also higher. Thus, lesser viable bacteria are present in the central regions.  
466 Viability studies on realistic biofluids like respiratory fluid droplets also show a similar trend.  
467 A detailed study using actual biofluids is required to understand the phenomena better for  
468 practical applications.

469

## 470 **Methods**

### 471 **Bacterial culture and cell line maintenance:**

472 The bacterial culture of *Klebsiella pneumoniae* (KP) was cultured in Luria Bertani (LB) broth  
473 overnight at 175 rpm shaker and 37°C incubators. The overnight grown (stationary phase)  
474 bacteria were washed five times with Milli-Q water to remove any remnants of the LB media  
475 and then resuspended in either Milli-Q water or SRF as mentioned in the particular experiment.  
476 For the Log phase, bacterial culture, the bacteria were sub-cultured at 1:33 ratio of bacteria:  
477 fresh media and incubated for 2 hours further at 37°C incubator shakers. For staining with a  
478 membrane dye called FM 4-64, the bacteria from stationary or log phase were incubated at the  
479 ice with dye in milliQ (at a concentration 1µg/mL of FM 4-64) for about 15mins, and bacterial  
480 cells were further washed with Milli-Q to remove excess dye and resuspended in Milli-Q or  
481 SRF as mentioned in a given experiment.

482 Murine macrophages were cultured in Dulbecco's Modified Eagle's Media (DMEM)  
483 containing 10% FBS at 37 °C incubator with 5% CO<sub>2</sub>. 12 hours prior to infection experiments,  
484 cells were seeded in 24 well plate at a confluency of 70-80%.

### 485 **Bacterial Viability and Gentamicin Protection Assay:**

486 The dried droplet, either whole droplet (W), edge removed (ER), or center removed (CR), was  
487 resuspended in PBS, and then the resuspended bacteria were plated onto LB agar to an  
488 enumerated viable bacterial number and was also used to infect in RAW264.7 macrophages,  
489 the cells were then centrifuged at 700rpm to increase the adherence of bacteria to mammalian  
490 cells. Next, the bacteria were incubated at 37°C incubators with 5% CO<sub>2</sub>. The cells were  
491 washed after 30mins with PBS, and media was removed and fresh media added containing  
492 100ug/mL of gentamicin; further, after 1hour, media was removed and fresh media containing  
493 25ug/mL of gentamicin. At 2hours and 16 hours post-infection, the mammalian cells were  
494 lysed and plated onto an LB agar plate to enumerate bacterial numbers at specific timepoints.

#### 495 **Droplet Evaporation:**

496 The Surrogate respiratory fluid is prepared according to the procedure mentioned in Rasheed  
497 et.al.<sup>52</sup>The bacteria suspended in Milli-Q and SRF droplets are casted on the glass substrate  
498 cleaned with Isopropyl alcohol. During the experiments, ambient conditions are maintained at  
499 the relative humidity  $50 \pm 3\%$  and temperature  $27 \pm 1^\circ\text{C}$ . Droplets of volume  $0.95 \pm 0.1 \mu\text{l}$  are  
500 drop cast on glass substrates cleaned with Isopropyl alcohol. The droplets showed an initial  
501 contact angle of  $46 \pm 2^\circ$ ; the droplet dries in pinned contact line mode with a wetting diameter  
502 of  $2.2 \pm 0.07 \text{ mm}$ . The bacterial motion and deposition near the end of evaporation are recorded  
503 using the bright and dark field optical method.

504 A bright-field image of the final deposition pattern is recorded using a DSLR camera. Scanning  
505 electron microscopy imaging reveals the finer details of the deposition and the arrangement of  
506 bacteria.

#### 507 **Cell imaging and live tracking**

508 The bacterial motion is tracked using membrane stain FM 4-63 with a excitation/emission  
509 maximum of 515/640 nm at 2.28 fps using a Leica TCS SP8 microscope.

#### 510 **Micro-Particle Image Velocimetry ( $\mu$ -PIV)**

511 The  $\mu$ -PIV technique is used to qualitatively and quantitatively study the flow inside droplets.  
512 Neutrally buoyant monodisperse (of size  $860 \pm 5 \text{ nm}$ ) fluorescent polystyrene particles are used  
513 for  $\mu$ -PIV experiments. The polystyrene particles mentioned above were procured from  
514 ThermoFisher Scientific. These fluorescent polystyrene particles are added to the bacteria-  
515 containing liquid at 0.008% by volume. These polystyrene particles faithfully follow the flow

516 as their stokes number is (St)  $St = \frac{\rho_p d_p^2 U_c}{18\mu_f L_c} \sim O(10^{-12}) \ll 1$ . Where,  $\rho_p$  is the particle density,  
517  $d_p$  is the diameter of the particle,  $\mu_f$  is the fluid viscosity,  $L_c$  is the characteristic length scale  
518 ( $\sim$ contact diameter of the droplet),  $U_c$  is the expected velocity scale. The droplet containing  
519 bacteria (non-fluorescent) and polystyrene particles (fluorescent) is volumetrically illuminated  
520 using an Nd: Yag laser (NanoPIV, Litron Laser). Images are captured from the bottom of the  
521 solvent droplet using an Imager Intense camera fitted to a Flowmaster MITAS microscope  
522 [Field of View:  $1000 \times 600 \mu\text{m}^2$ , depth of field:  $28 \mu\text{m}$ ]. The images are acquired at 1 *fps* using  
523 a single frame–single pulse technique. The particles move 3-4 pixels in the subsequent frames,  
524 optimal for PIV computation. All images are pre-processed by applying appropriate  
525 background subtraction. Post-processing is done by pair-wise cross-correlation of sequential  
526 single-frame images. The interrogation window is maintained at  $64 \times 64$  pixels for the first  
527 pass and  $32 \times 32$  pixels for the subsequent passes with 50% overlap between two windows.  
528 The instantaneous vector fields thus obtained are temporally averaged (over the time period  
529 pertaining to each regime) to obtain the final velocity vectors. The above post-processing of  
530 images is done using DaVis7.2 software from LaVision GmbH.

### 531 **Atomic force Microscopy**

532 Park NX10 atomic force microscope is used to obtain the images and force distance  
533 spectroscopy analysis. The CONTSCR probe with 0.2 N/m stiffness is used for the  
534 measurements. The nanoindentation is done at the speed of  $0.3 \mu\text{m/s}$  for both up and down  
535 directions without holding.

### 536 **Credit statement**

537 Conceptualization: S.B. and D.C.; Methodology: S.B., D.C., A.R., O.H., R.C., S.R.S.;  
538 Investigation: A.R., O.H., R.C., S.R.S.; Visualization: A.R., O.H., R.C., S.R.S.; Funding  
539 acquisition: D.C. and S.B.; Project administration: D.C. and S.B.; Supervision: D.C. and S.B.;  
540 Writing— original draft: A.R., O.H., R.C., S.R.S.; Writing: A.R., O.H., R.C., S.R.S.; editing  
541 and revision: S.B., D.C., A.R., O.H., R.C., S.R.S.

542

### 543 **Data availability statement**

544 All relevant data are within the paper and its Supporting Information files. All materials and  
545 additional data are available from the corresponding author upon request.

546

547

548 **References**

- 549 1. Rusconi, R., Guasto, J. S. & Stocker, R. Bacterial transport suppressed by fluid shear. *Nature*  
550 *Physics* 2014 10:3 **10**, 212–217 (2014).
- 551 2. Mathijssen, A. J. T. M. *et al.* Oscillatory surface rheotaxis of swimming E. coli bacteria. *Nature*  
552 *Communications* 2019 10:1 **10**, 1–12 (2019).
- 553 3. Secchi, E. *et al.* The effect of flow on swimming bacteria controls the initial colonization of  
554 curved surfaces. *Nature Communications* **11**, 1–12 (2020).
- 555 4. Vizsnyiczai, G. *et al.* A transition to stable one-dimensional swimming enhances E. coli  
556 motility through narrow channels. *Nature Communications* 2020 11:1 **11**, 1–7 (2020).
- 557 5. Kannan, A., Yang, Z., Kim, M. K., Stone, H. A. & Siryaporn, A. Dynamic switching enables  
558 efficient bacterial colonization in flow. *Proceedings of the National Academy of Sciences* **115**,  
559 5438–5443 (2018).
- 560 6. Dalwadi, M. P. & Pearce, P. Emergent robustness of bacterial quorum sensing in fluid flow.  
561 *Proceedings of the National Academy of Sciences* **118**, (2021).
- 562 7. Guasto, J. S., Rusconi, R. & Stocker, R. Fluid mechanics of planktonic microorganisms. *Annual*  
563 *Review of Fluid Mechanics* **44**, 373–400 (2011).
- 564 8. Stoodley, P., Lewandowski, Z., Boyle, J. D. & Lappin-Scott, H. M. The formation of migratory  
565 ripples in a mixed species bacterial biofilm growing in turbulent flow. *Environ Microbiol* **1**,  
566 447–455 (1999).
- 567 9. Bengtsson-Palme, J., Kristiansson, E. & Larsson, D. G. J. Environmental factors influencing the  
568 development and spread of antibiotic resistance. *FEMS Microbiology Reviews* **42**, 68–80  
569 (2018).
- 570 10. Peirano, G., Chen, L., Kreiswirth, B. N. & Pitouta, J. D. D. Emerging antimicrobial-resistant  
571 high-risk klebsiella pneumoniae clones ST307 and ST147. *Antimicrobial Agents and*  
572 *Chemotherapy* **64**, (2020).
- 573 11. Wyres, K. L. & Holt, K. E. Klebsiella pneumoniae as a key trafficker of drug resistance genes  
574 from environmental to clinically important bacteria. *Current Opinion in Microbiology* **45**, 131–  
575 139 (2018).
- 576 12. Landman, D. *et al.* Evolution of antimicrobial resistance among Pseudomonas aeruginosa,  
577 Acinetobacter baumannii and Klebsiella pneumoniae in Brooklyn, NY. *Journal of Antimicrobial*  
578 *Chemotherapy* **60**, 78–82 (2007).
- 579 13. Tang, J. W., Li, Y., Eames, I., Chan, P. K. S. & Ridgway, G. L. Factors involved in the aerosol  
580 transmission of infection and control of ventilation in healthcare premises. *Journal of Hospital*  
581 *Infection* **64**, 100–114 (2006).
- 582 14. Esteves, D. C. *et al.* Influence of biological fluids in bacterial viability on different hospital  
583 surfaces and fomites. *American Journal of Infection Control* **44**, 311–314 (2016).
- 584 15. Majee, S. *et al.* Spatiotemporal evaporating droplet dynamics on fomites enhances long term  
585 bacterial pathogenesis. *Communications Biology* 2021 4:1 **4**, 1–16 (2021).

- 586 16. Xie, X., Li, Y., Zhang, T. & Fang, H. H. P. Bacterial survival in evaporating deposited droplets on  
587 a teflon-coated surface. *Applied Microbiology and Biotechnology* **73**, 703–712 (2006).
- 588 17. Kramer, A., Schwebke, I. & Kampf, G. How long do nosocomial pathogens persist on  
589 inanimate surfaces? A systematic review. *BMC Infectious Diseases* **6**, 1–8 (2006).
- 590 18. Xie, X., Li, Y., Zhang, T. & Fang, H. H. P. Bacterial survival in evaporating deposited droplets on  
591 a teflon-coated surface. *Applied Microbiology and Biotechnology* **73**, 703–712 (2006).
- 592 19. Huang, Q., Wang, W. & Vikesland, P. J. Implications of the Coffee-Ring Effect on Virus  
593 Infectivity. *Langmuir* **37**, 11260–11268 (2021).
- 594 20. Alsved, M. *et al.* Effect of Aerosolization and Drying on the Viability of *Pseudomonas syringae*  
595 Cells. *Frontiers in Microbiology* **9**, 3086 (2018).
- 596 21. Tugba Andac *et al.* Active matter alters the growth dynamics of coffee rings. *Soft Matter* **15**,  
597 1488–1496 (2019).
- 598 22. van Loosdrecht, M. C., Lyklema, J., Norde, W., Schraa, G. & Zehnder, A. J. The role of bacterial  
599 cell wall hydrophobicity in adhesion. *Applied and Environmental Microbiology* **53**, 1893  
600 (1987).
- 601 23. Di Martino, P., Cafferini, N., Joly, B. & Darfeuille-Michaud, A. *Klebsiella pneumoniae* type 3 pili  
602 facilitate adherence and biofilm formation on abiotic surfaces. *Res Microbiol* **154**, 9–16  
603 (2003).
- 604 24. Marín, Á. G., Gelderblom, H., Lohse, D. & Snoeijer, J. H. Order-to-disorder transition in ring-  
605 shaped colloidal stains. *Physical Review Letters* **107**, (2011).
- 606 25. Dugyala, V. R. & Basavaraj, M. G. Evaporation of sessile drops containing colloidal rods:  
607 Coffee-ring and order-disorder transition. *Journal of Physical Chemistry B* **119**, 3860–3867  
608 (2015).
- 609 26. Marín, Á. G., Gelderblom, H., Lohse, D. & Snoeijer, J. H. Order-to-Disorder Transition in Ring-  
610 Shaped Colloidal Stains. *Physical Review Letters* **107**, 085502 (2011).
- 611 27. Nocker, A., Fernández, P. S., Montijn, R. & Schuren, F. Effect of air drying on bacterial  
612 viability: A multiparameter viability assessment. *Journal of Microbiological Methods* **90**, 86–  
613 95 (2012).
- 614 28. Alsved, M. *et al.* Effect of Aerosolization and Drying on the Viability of *Pseudomonas syringae*  
615 Cells. *Frontiers in Microbiology* **9**, (2018).
- 616 29. Xie, X., Li, Y., Zhang, T. & Fang, H. H. P. Bacterial survival in evaporating deposited droplets on  
617 a teflon-coated surface. *Applied Microbiology and Biotechnology* **73**, 703–712 (2006).
- 618 30. Pazos-Rojas, L. A. *et al.* Desiccation-induced viable but nonculturable state in *Pseudomonas*  
619 *putida* KT2440, a survival strategy. *PLoS ONE* **14**, (2019).
- 620 31. Greffe, V. R. G. & Michiels, J. Desiccation-induced cell damage in bacteria and the relevance  
621 for inoculant production. *Applied Microbiology and Biotechnology* vol. 104 3757–3770 (2020).
- 622 32. Deegan, R. D. *et al.* Capillary flow as the cause of ring stains from dried liquid drops. *Nature*  
623 *(London)* **389**, 827–829 (1997).



- 624 33. Baughman, K. F. *et al.* Evaporative deposition patterns of bacteria from a sessile drop: effect  
625 of changes in surface wettability due to exposure to a laboratory atmosphere. *Langmuir* **26**,  
626 7293–7298 (2010).
- 627 34. Ranjbaran, M. & Datta, A. K. Retention and infiltration of bacteria on a plant leaf driven by  
628 surface water evaporation. *Physics of Fluids* **31**, 112106 (2019).
- 629 35. Agrawal, A., Sinha, S., Mukherjee, R. & Mampallil, D. Dynamics of bacterial deposition in  
630 evaporating drops. *Physics of Fluids* **32**, 093308 (2020).
- 631 36. Wheeler, J. D., Secchi, E., Rusconi, R. & Stocker, R. Not just going with the flow: The effects of  
632 fluid flow on bacteria and plankton. *Annual Review of Cell and Developmental Biology* vol. 35  
633 213–237 (2019).
- 634 37. Dugyala, V. R. & Basavaraj, M. G. Evaporation of sessile drops containing colloidal rods:  
635 Coffee-ring and order-disorder transition. *Journal of Physical Chemistry B* **119**, 3860–3867  
636 (2015).
- 637 38. Sefiane, K. Patterns from drying drops. *Advances in Colloid and Interface Science* **206**, 372–  
638 381 (2014).
- 639 39. Marín, Á. G., Gelderblom, H., Lohse, D. & Snoeijer, J. H. Order-to-disorder transition in ring-  
640 shaped colloidal stains. *Physical Review Letters* **107**, 085502 (2011).
- 641 40. Cefali, E. *et al.* *Morphologic Variations in Bacteria under Stress Conditions: Near-Field Optical*  
642 *Studies*. vol. 24 (2002).
- 643 41. Deng, Y., Sun, M. & Shaevitz, J. W. Direct measurement of cell wall stress stiffening and turgor  
644 pressure in live bacterial cells. *Physical Review Letters* **107**, 7–10 (2011).
- 645 42. Green, E. R. & Meccas, J. Bacterial Secretion Systems: An Overview. *Microbiology Spectrum* **4**,  
646 (2016).
- 647 43. Hooda, Y. *et al.* Slam is an outer membrane protein that is required for the surface display of  
648 lipidated virulence factors in *Neisseria*. *Nat Microbiol* **1**, 16009 (2016).
- 649 44. Jiran, E. & Thompson, C. v. Capillary instabilities in thin films. *Journal of Electronic Materials*  
650 **19**, 1153–1160 (1990).
- 651 45. Velev, O. D. *et al.* Mechanism of formation of two-dimensional crystals from latex particles on  
652 substrata. *Progress in Colloid & Polymer Science* **93**, 366–367 (1993).
- 653 46. Sur, J. & Pak, H. K. Capillary force on colloidal particles in a freely suspended liquid thin film.  
654 *Physical Review Letters* **86**, 4326–4329 (2001).
- 655 47. Jr, T., J Opt, J. W., Denkov, N. D., Velev A Kralchevsky I B Ivanov, D. P. & Yoshimura Nagayama,  
656 H. K. Two-dimensional crystallization Checkpoint check. *Nagayama, K. Nanobiology* **44**, 25–37  
657 (1954).
- 658 48. Habibi, M., Moller, P., Fall, A., Rafai, S. & Bonn, D. Pattern formation by dewetting and  
659 evaporating sedimenting suspensions. *Soft Matter* **8**, 4682–4686 (2012).
- 660 49. Kralchevsky, P. A. & Denkov, N. D. Capillary forces and structuring in layers of colloid  
661 particles. *Current Opinion in Colloid and Interface Science* **6**, 383–401 (2001).

- 662 50. Malla, L. K., Bhardwaj, R. & Neild, A. Analysis of profile and morphology of colloidal deposits  
663 obtained from evaporating sessile droplets. *Colloids and Surfaces A: Physicochemical and*  
664 *Engineering Aspects* **567**, 150–160 (2019).
- 665 51. Majee, S. *et al.* Spatiotemporal evaporating droplet dynamics on fomites enhances long term  
666 bacterial pathogenesis. *Communications Biology* **4**, (2021).
- 667 52. Rasheed, A. *et al.* Precipitation dynamics of surrogate respiratory sessile droplets leading to  
668 possible fomites. *Journal of Colloid and Interface Science* **600**, 1–13 (2021).
- 669
- 670